Colloidal Platinum–Copper Nanocrystal Alloy Catalysts Surpass Platinum in Low-Temperature Propene Combustion

Nadia Tahsini, An-Chih Yang, Verena Streibel, Baraa Werghi, Emmett D. Goodman, Aisulu Aitbekova, Simon R. Bare, Yuejin Li, Frank Abild-Pedersen, and Matteo Cargnello*

ABSTRACT: Low-temperature removal of noxious environmental emissions plays a critical role in minimizing the harmful effects of hydrocarbon fuels. Emission-control catalysts typically consist of large quantities of rare, noble metals (e.g., platinum and palladium), which are expensive and environmentally damaging metals to extract. Alloying with cheaper base metals offers the potential to boost catalytic activity while optimizing the use of noble metals. In this work, we show that Pt_xCu_{100-x} catalysts prepared from colloidal nanocrystals are more active than the corresponding Pt catalysts for complete propene oxidation. By carefully controlling their composition while maintaining nanocrystal size, alloys with dilute Cu concentrations (15–30% atomic fraction) demonstrate promoted activity compared to pure Pt. Complete propene oxidation was observed at temperatures as low as 150 °C in the presence of steam, and five to ten times higher turnover frequencies were found compared to monometallic Pt catalysts. Through DFT studies and structural and catalytic characterization, the remarkable activity of dilute Pt_xCu_{100-x} alloys was related to the tuning of the electronic structure of Pt to reach optimal binding energies of C* and O* intermediates. This work provides a general approach toward investigation of structure–property relationships of alloyed catalysts with efficient and optimized use of noble metals.

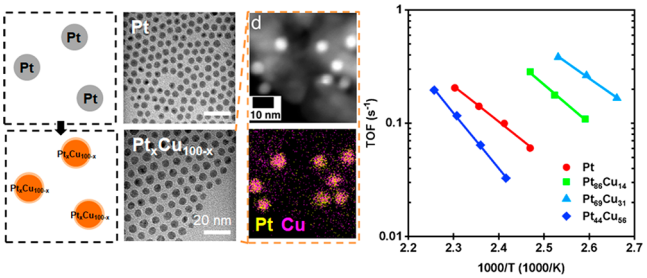

INTRODUCTION

As scientists develop ways to limit air pollution, reducing atmospheric emissions of toxic compounds plays an important role in long-term environmental remediation strategies.[1] A significant source of emissions comes from automobile combustion engines, and hydrocarbons are one of the major components. Many countries worldwide have established increasingly stringent regulations on hydrocarbon emissions. To meet the requirements, advances in catalytic combustion, which remains the most economically efficient way to avoid hydrocarbon emissions, must be continuously produced.[2,3] In recognition of this need, the U.S. Department of Energy suggested the 150 °C challenge as a way to identify efficient emission control catalysts that achieve 90% conversion of emissions below 150 °C.[4] This need is further justified by the development of more efficient engines that operate at lower temperatures. Catalysts to limit hydrocarbon emissions are needed with high activity at the low temperatures of exhaust emissions.[5,6] Additionally, many of the best performing catalysts utilize large amounts of noble metals, such as platinum and palladium.[5,7−9] The high price and environmental toll of extracting these metals are problematic, and cheaper and more environmentally friendly solutions are required.[10]

Propene is used as a model compound in studying emission control catalysts as it is one of the most abundant hydrocarbons emitted.[11] Existing studies of complete oxidation of propene have focused largely on platinum catalysts due to their relatively high activity.[12] Various structural parameters of supported platinum catalysts have been investigated, such as nanocrystal (NC) size,[13−15] phase,[16] metal–support interaction,[12,17] and composition effect.[18,19] Yet, despite the existing work on Pt-based catalysts for propene combustion, there have been no studies identifying effective alloy catalysts that replace Pt with base metals. This direction is appealing to both reduce the amount of precious metals used as well as explore new chemistries to improve catalytic performance for the oxidation of CO and hydrocarbons.[20−25]

In this work, we developed a seed-mediated approach to synthesize monodisperse Pt_xCu_{100-x} nanocrystal alloys with controlled Pt/Cu ratios. The Pt_xCu_{100-x} nanocrystals were supported on Al_2O_3 and studied for propene combustion in the

presence of steam, conditions relevant to emission control applications. Remarkably, some Pt_xCu_{100-x} alloys demonstrated complete propene combustion activity at 50 °C lower temperature than pure Pt. Rate order analyses indicated that Pt_xCu_{100-x} alloys of dilute Cu contents bind propene more strongly than pure Pt, resulting in facilitated activation of propene. These catalysts prove that, with the optimal Pt/Cu ratio, cheaper base metals can improve the catalytic activity of noble metal catalysts.

EXPERIMENTAL SECTION

Synthesis of 5 nm Pt Nanocrystals. All syntheses were performed using standard air-free Schlenk techniques, with slight modification of a previously reported procedure (see Supporting Information).[26]

Synthesis of Bimetallic Pt/Cu NCs. Pt_xCu_{100-x} nanocrystals with varying Pt/Cu ratios were synthesized by a seed-mediated alloying approach. In a three-neck flask, a volume of solution corresponding to 0.1 mmol of Pt NCs was combined with variable quantities of copper(II) acetylacetonate ($Cu(acac)_2$, 97%, Sigma-Aldrich) to achieve the desired Pt/Cu ratio (see Table S1 for further details). Oleylamine (OLAM, 8 mL) was added to the flask, and the mixture was placed under magnetic stirring and evacuated at 60 °C for 30 min. The reaction vessel was then flushed with nitrogen and heated quickly (~40 °C min^{-1}) to 280 °C. After 30 min of reaction, the solution was cooled rapidly to room temperature. The NCs were isolated by three rounds of precipitation using isopropanol and ethanol as antisolvents and separated by centrifugation (8000 rpm, 3 min). Finally, the NCs were dispersed in hexanes (~5 mL), including the addition of OLAM (~20 μL) for colloidal stability. NCs were rapidly impregnated onto supports to prevent any leaching of base metal into the solution.

Preparation of Catalyst Powders. Catalysts were prepared by impregnation of NC solutions onto support powders (see Supporting Information). All samples were fast-treated at 700 °C for 30 s in a furnace to remove ligands from synthesis, following a reported procedure.[27]

Microscopy Techniques. Transmission electron microscopy (TEM) images were recorded on an FEI Tecnai transmission electron microscope equipped with an Orius CCD camera operating at 200 kV. High-angle annular dark-field scanning transmission electron microscopy (HAADF-STEM) and energy-dispersive X-ray spectroscopy (EDS) mapping were performed on a TitanX operating at 300 kV at the National Center for Electron Microscopy at Lawrence Berkeley National Laboratory. EDS maps were taken on a TitanX equipped with a SuperEDS detector consisting of four windowless silicon drift detectors with a total solid angle of 0.7 steradians. Maps were acquired at 330 pA, and acquisition times were no longer than 5 min to minimize beam damage. The EDS spectrum quantification was performed via the Cliff–Lorimer method at the Pt–L edge and Cu–K edges.[28] NC samples were dropcast onto TEM grids from their native hexane solutions onto ultrathin carbon films supported on Ni mesh grids. It is important to note the use of Ni TEM grids to avoid a spurious Cu signal from the common C/Cu TEM grids. Supported catalyst TEM grids were prepared via dry deposition by carefully shaking a lacey-carbon Ni-mesh grid with catalyst powder in a plastic tube.

Additional Structural Characterization. X-ray photoelectron spectroscopy (XPS), CO chemisorption, and inductively coupled plasma optical emission spectroscopy (ICP-OES) characterization details are reported in the Supporting Information.

Catalytic Characterization Techniques. For light-off curves, an appropriate amount of catalyst (20–35 mg, keeping the Pt mass constant across all samples) was physically mixed with an alumina diluent to achieve 200 mg of total powder, thereby operating at a dilution ensuring neither mass nor thermal diffusion affected the catalytic results. The mixture was packed between silica sand layers in a U-shaped quartz microreactor with an internal diameter of 10 mm, and the reactor was mounted in a Micromeritics Eurotherm 2416 furnace. The sample was pretreated at 300 °C under O_2 (5 vol % in Ar) for 30 min, Ar for 10 min, and H_2 (5 vol % in Ar) for 30 min, all at 45 mL min^{-1}. The sample was then cooled under Ar to 100 °C, and the propene combustion reaction mixture was introduced. The reaction mixture consisted of 0.15 vol % C_3H_6, 3 vol % O_2, 10.4 vol % H_2O, balance Ar, with gas hourly space velocity (GHSV) held at 150 000 mL $g_{catalyst}^{-1}$ h^{-1}, and total flow rate of 49 mL min^{-1}. H_2O vapor was introduced into the gas stream by heating a water saturator to 47 °C. The sample was then heated to 500 °C at 10 °C min^{-1} and cooled to room temperature under the reaction mixture. Gas concentrations were monitored using a quadrupole mass spectrometer (Hiden Analytical HPR20) equipped with a Faraday detector, following the parent molecular ions for C_3H_6 (41 amu), O_2 (32 amu), CO_2 (44 amu), and H_2O (18 amu). Light-off curves were smoothed and plotted using a five-period moving average.

For kinetic experiments, 22 mg of catalyst was physically mixed with alumina diluent to achieve 200 mg of total powder. Kinetic measurements were conducted using the same pretreatment conditions described for light-off experiments. The same reaction mixture was maintained from light-off experiments, but the final conversion was kept below 10% to ensure differential conditions. Gas concentrations were monitored by a gas chromatograph (Buck Scientific model 910) using a flame ionization detector (FID) with a methanizer and thermal conductivity detector (TCD) with Ar as the carrier gas.

For rate order measurements, 22 mg of catalyst was physically mixed with alumina diluent to achieve 200 mg of total powder. Measurements were conducted using the same pretreatment conditions described above. Rate order measurements were conducted below 10% conversion at constant temperature (136 ± 2 °C). The feed consisted of 0.15 vol % C_3H_6, 3 vol % O_2, 10.4 vol % H_2O, and balance Ar, while the partial pressures of C_3H_6 and O_2 were varied separately. The C_3H_6 concentration was varied between 0.1 vol % and 0.6 vol % and O_2 between 1 vol % and 4.5 vol %.

X-ray Absorption Spectroscopy (XAS). X-ray absorption spectroscopy spectra were collected at beamline 9–3 at Stanford Synchrotron Radiation Lightsource at SLAC National Accelerator Laboratory. Beamline 9–3 is a 16-pole, 2-T wiggler beamline with a vertically collimating mirror for harmonic rejection and a cylindrically bent mirror for focusing. The photon energy was selected using a liquid-nitrogen-cooled, double-crystal Si (220) monochromator (crystal orientation = 90°). The ion chambers were filled with N_2 gas for the Pt L_3-edge. The catalyst samples (0.37 wt % $Pt_{69}Cu_{31}/Al_2O_3$ fresh and postcatalysis pretreated in O_2 at 300 °C for 30 min, Ar for 10 min, and then reduction with 5 vol % H_2 for 30 min; the pretreatment is followed by exposure to a propene combustion mixture at 150 °C for 12 h) were prepared for ex situ XAS measurements. About 20 mg of each of the samples was packed in a 3 mm capillary tube. The XAS data were collected in fluorescence yield mode using a PIPS detector orthogonal (90°) to the beam path with a Soller slit. The beam size of 1 mm [v] by 2 mm [h] was used. A total of 9 scans were collected to improve the signal/noise ratio. A Pt foil reference was scanned simultaneously for energy calibration.

The raw XAS spectra were energy-calibrated, merged, and normalized and background subtracted using the Athena software. Then the fitting was conducted using the Artemis interface of the Demeter software package.[29] The models only include single scattering paths, and the relevant scattering paths were calculated using FEFF6 from the crystallographic information file (CIF) of Pt–Cu-mp-644311. S_0^2 was determined to be 0.81 ± 0.03 for the Pt L3-edge from fitting Pt foil (Figure S8). The EXAFS data for the 5 nm $Pt_{69}Cu_{31}/Al_2O_3$ samples were modeled simultaneously to minimize statistical errors. The simultaneous fits shared the same σ^2 and E_0 values for the Pt–Cu and Pt–Pt scattering paths.

With the interest to determine the mixing behavior and alloying structure within this system, we applied a methodology developed by Frenkel et al. where EXAFS data were used to extract the Cowley's short-range order parameter (defined by eq 1).[30–32]

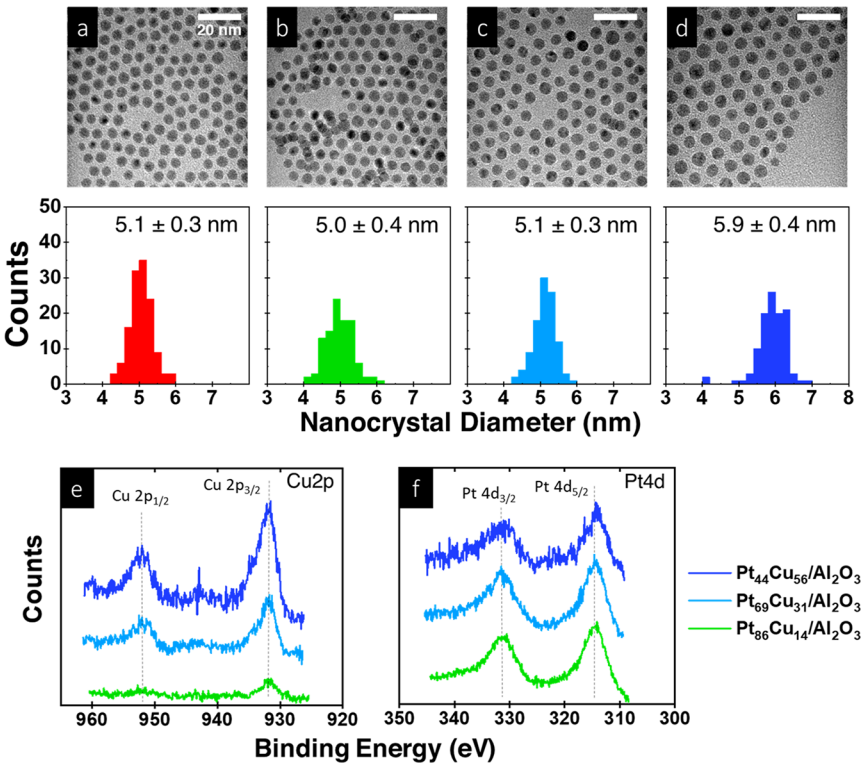

Figure 1. (a–d) Representative TEM images and particle size distributions of as-synthesized nanocrystals: (a) Pt; (b) $Pt_{86}Cu_{14}$; (c) $Pt_{69}Cu_{31}$; and (d) $Pt_{44}Cu_{56}$. All scale bars are 20 nm. (e,f) XPS spectra of Pt_xCu_{100-x}/Al_2O_3 catalysts: (e) Cu 2p and (f) Pt 4d. XPS spectra intensities normalized to ensure similar Pt signals.

$$\alpha_{Pt-Cu} = 1 - \left(\frac{N_{Pt-Cu}/N_{Pt}}{x_{Cu}} \right) \quad (1)$$

with $x_{Pt} + x_{Cu} = 1$and $N_{Pt-Cu} \times x_{Pt} = N_{Cu-Pt} \times x_{Cu}$ where N_{Pt-Cu} is the coordination number of Pt–Cu atoms; N_{Cu-Pt} is the coordination number of Cu–Pt atoms; N_{Pt} is the coordination number of Pt atoms; x_{Cu} is the atomic fraction of Cu; and x_{Pt} is the atomic fraction of Pt.

COMPUTATIONAL SECTION

We performed first-principles, periodic DFT studies using the Quantum ESPRESSO (QE) package[33] implemented within the Atomic Simulation Environment (ASE).[34] We computed self-consistent energies with the BEEF-vdW exchange-correlation functional.[35] The BEEF-vdW functional has been benchmarked to describe both van der Waals interactions of adsorbates and chemisorption on surfaces. Ultrasoft Vanderbilt pseudopotentials[36] were used to represent ionic core states, and the Monkhorst–Pack method[37] was employed to generate k-point grids inside the Brillouin zone.

For all gas-phase, slab, and bulk calculations, we used kinetic energy cutoffs for plane waves and charge densities of 500 and 5000 eV, respectively. To ease convergence of the Kohn–Sham equations, electronic states were smeared by 0.1 eV using a Gaussian distribution. We converged total energies to at least 10^{-5} eV and forces on atoms to below 0.05 eV/Å.

To determine the equilibrium lattice constants of Pt_3Cu, PtCu, and $PtCu_3$ alloys, we retrieved structures from materialsproject.org[38] and optimized them with several iterations of vc-relax within QE on a 12 × 12 × 12 k-point grid. For the lattice constants of fcc Pt and Cu, the equation of state method was used on a 12 × 12 × 12 k-point grid. The obtained lattice constants are Pt_3Cu: a = 3.94 Å; PtCu: $a = b$ = 3.96 Å, c = 3.68 Å; $PtCu_3$: a = 3.77 Å; Pt: a = 3.98 Å; Cu: a = 3.66 Å.

For surface calculations, we used four-layered 3 × 3 Pt and Cu (211) surface slabs, as well as four-layered 3 × 4 Pt_3Cu, PtCu, and $PtCu_3$ (211) surface slabs. For these slabs, the atoms in the bottom three layers were fixed to their bulk positions, while the top-layer atoms and the adsorbates were relaxed. We self-consistently solved the Kohn–Sham equations on a 4 × 4 × 1 k-point grid in reciprocal space. At least 14 Å of vacuum separated the periodic images of surface slabs. Further, to mitigate spurious interaction between the periodic images, we applied dipole corrections[39] perpendicular to the slab surface. To calculate the density of states projected on the Pt and Cu step atoms, we used a denser sampling grid of 6 × 6 × 1 k-points.

For gas-phase calculations, we computed the total energies of molecules in 21 Å × 22 Å × 23 Å unit cells at the gamma point. Since some gas-phase species are poorly described by the used BEEF-vdW exchange-correlation functional as detailed elsewhere,[40,41] we adopted the following correction: H_2 + 0.09 eV. We referenced all adsorption energies to the (corrected) gas-phase energies of CH_4, H_2O, and H_2. We used VESTA[42] to generate images of atomic structures.

RESULTS AND DISCUSSION

Monodisperse bimetallic platinum/copper nanocrystals were colloidally synthesized via a seed-mediated growth approach (Scheme S1). Following the preparation of monometallic ~5 nm Pt nanocrystals (NCs), they were used as seeds and combined with varying amounts of $Cu(acac)_2$ to prepare highly uniform Pt_xCu_{100-x} NCs (where x denotes atomic content) with controlled Pt/Cu ratios (Table S1). Figure 1

shows representative TEM images and particle size distributions that confirm the uniformity of the NC sizes obtained via this synthetic approach (σ < 10% for each sample). A slight increase in average particle size for the Cu-rich alloy to 5.9 nm was observed. Cu-rich Pt/Cu systems may crystallize in a rhombohedral lattice structure,[43] which has lower atom packing efficiency (52−74%) compared to other Pt-rich Pt/Cu systems (74%, FCC type). The increase in particle size from Pt to Cu-rich Pt/Cu (16%) can thus be explained by the change in crystal structure with correspondingly lower atom packing efficiency.[43,44] Three NC compositions were prepared: $Pt_{86}Cu_{14}$, $Pt_{69}Cu_{31}$, and $Pt_{44}Cu_{56}$, where the subscript signifies the atomic percentage of the element as given by inductively coupled plasma optical emission spectroscopy (ICP-OES). ICP-OES analysis and energy-dispersive X-ray spectroscopy (EDS) mapping of the NCs confirmed the metal contents and the presence of both metals in each individual NC (Table 1).

Table 1. Quantitative Bulk ICP and EDS Analysis of Pt and Pt_xCu_{100-x} NCs Prepared in This Work

	ICP Pt content	ICP Cu content	EDS Pt content	EDS Cu content
Pt	99.8%	0.2%	>90%	<10%[a]
low PtCu ($Pt_{86}Cu_{14}$)	86%	14%	79%	21%
medium PtCu ($Pt_{69}Cu_{31}$)	69%	31%	62%	38%
high PtCu ($Pt_{44}Cu_{56}$)	44%	56%	44%	56%

[a]Below detection limit.

The Pt/Cu metal ratios quantified from ICP-OES and EDS analysis were in good agreement with each other and with the Pt/Cu ratio used in the synthesis, demonstrating the ability to precisely control metal concentrations.

The Pt_xCu_{100-x} NCs, along with Pt as a reference, were used to make a library of supported 5 nm NC catalysts by deposition on γ-alumina used as support to prepare Pt/Al_2O_3, $Pt_{86}Cu_{14}/Al_2O_3$, $Pt_{69}Cu_{31}/Al_2O_3$, and $Pt_{44}Cu_{56}/Al_2O_3$. The metal loadings for all samples were maintained at ∼0.3 wt % including both Pt and Cu and were confirmed via ICP-OES analysis of the supported catalysts (Table S2). XPS of the final Pt_xCu_{100-x}/Al_2O_3 catalysts revealed increasing Cu/Pt ratios in the materials at increasing Cu content (Figure 1e,f), in line with the above ICP and EDS characterization. All samples revealed Pt and Cu signals at 314.4 and 932 eV, respectively, corresponding to metallic, reduced states.[45] These spectra suggest that Pt contributed to maintain Cu in a lower oxidation state despite the sample having been exposed to air.

The exposed metal surface area was determined by CO chemisorption (Table S2). It was observed that with increasing Cu content the exposed Pt surface area decreased, demonstrating that Cu is present on the surface of the NCs. Although Cu shows binding energy corresponding to the metallic state (see XPS data in Figure 1e) which should adsorb CO, it is possible that adding Cu induces geometric changes to the Pt surface that result in a different number of coordinated CO on PtCu surfaces.[46] Besides, metallic Cu is found to have weaker CO adsorption energy compared to noble metals;[47,48] therefore, we conclude that CO chemisorption provided an estimate of the exposed Pt surface.

Figure 2 and Figure S1 show the STEM EDS elemental mapping measurements and representative EDS spectrum in the catalysts, where Pt−L_3 and Cu−K signals were found to be evenly distributed across each individual NC, thus suggesting alloy formation. The change in EDS counts for Pt and Cu varied with the corresponding different Pt_xCu_{100-x} compositions. The Pt/Al_2O_3 sample (Figure 2a") showed no significant Cu signal beyond the background signal. These EDS maps confirmed the feasibility of the synthetic method to make

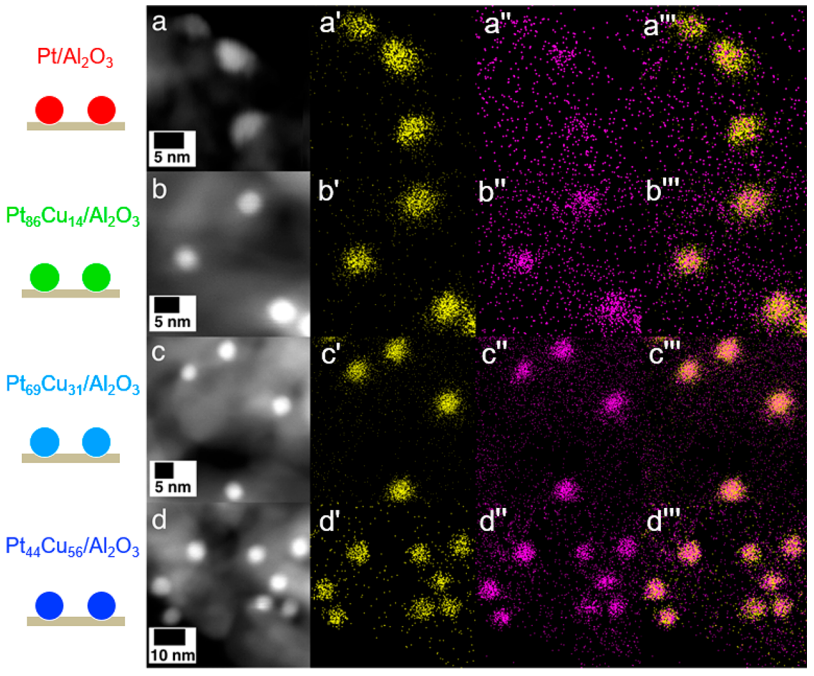

Figure 2. Representative HAADF-STEM images (a−d) and EDS-STEM mappings of the (a′−d′) Pt−L signal, (a″−d″) Cu−K signal, and (a‴−d‴) Pt−L/Cu−K signal overlay for (a) Pt/Al_2O_3, (b) $Pt_{86}Cu_{14}/Al_2O_3$, (c) $Pt_{69}Cu_{31}/Al_2O_3$, and (d) $Pt_{44}Cu_{56}/Al_2O_3$. The relatively strong Cu background signals are from stray fluorescence from the Cu present on the STEM column itself.

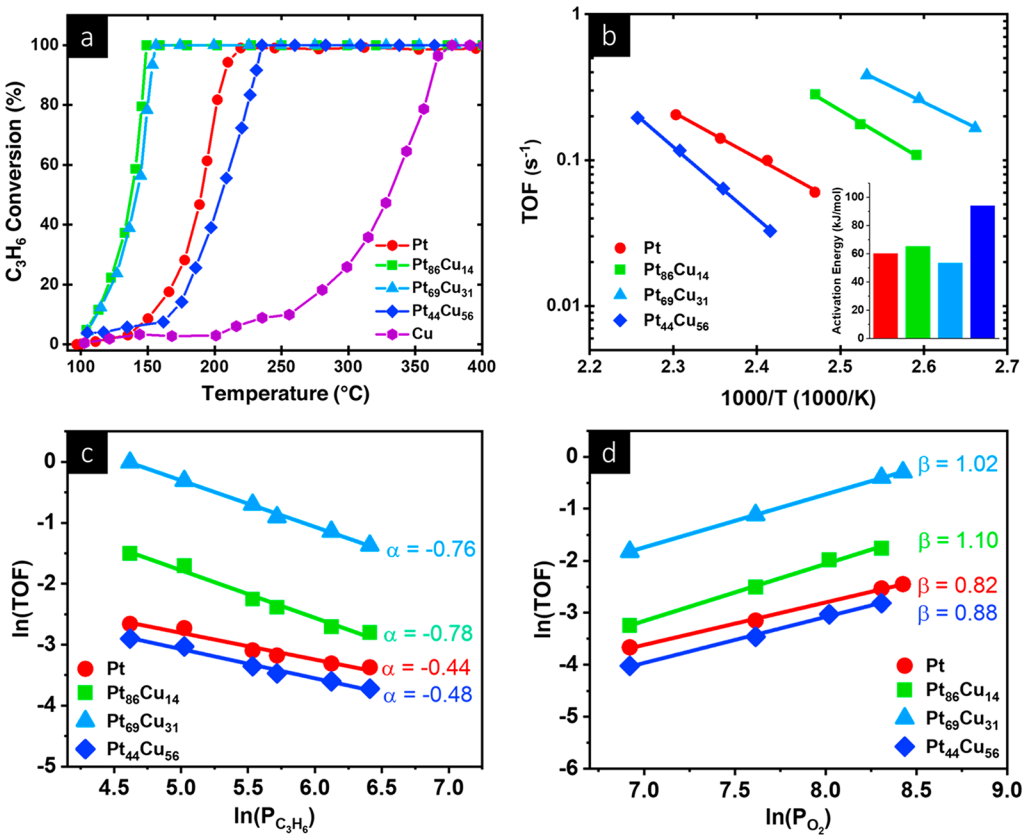

Figure 3. (a) Propene combustion light-off curves for Pt_xCu_{100-x}/Al_2O_3 catalysts. (b) Steady-state kinetic plot of turnover frequencies (TOFs) for Pt_xCu_{100-x}/Al_2O_3 catalysts, normalized to exposed Pt atoms. (c,d) Rate order measurements for Pt_xCu_{100-x}/Al_2O_3 catalysts; measurements shown for propene (c) and oxygen (d) rate orders. Reaction conditions for (a) and (b): 0.15 vol % C_3H_6, 3 vol % O_2, 10 vol % H_2O, balance Ar. For (c), reaction conditions varied C_3H_6 between 0.1 vol % and 0.6 vol % at 136 °C. For (d), reaction conditions varied O_2 between 1 vol % and 4.5 vol % at 136 °C.

tunable Pt_xCu_{100-x} nanocrystal catalysts with precise, uniform elemental composition.

In order to explore the effect of different Cu concentrations on propene combustion activity, both light-off curves and kinetic measurements in the presence of 10 vol % steam were collected. Light-off curves (Figure 3a) were used as an initial screening tool for different Pt_xCu_{100-x}/Al_2O_3 materials, and all experiments were normalized by using the same, constant mass of Pt in the reactor. The catalyst with the highest Cu loading, $Pt_{44}Cu_{56}/Al_2O_3$, was found to perform worse than the Pt/Al_2O_3 sample, with complete propene conversion occurring ~50 °C higher than pure Pt. Remarkably, the $Pt_{86}Cu_{14}/Al_2O_3$ and $Pt_{69}Cu_{31}/Al_2O_3$ catalysts exhibited improved performance over the monometallic Pt/Al_2O_3 catalyst. Both alloyed materials reached full propene conversion at 150 °C, which is 50 °C lower than the Pt/Al_2O_3 catalyst. As an important control experiment, a monometallic Cu/Al_2O_3 catalyst was also synthesized from Cu NCs and tested (Figure S2), but it displayed extremely low activity, with full propene conversion eventually achieved only above 375 °C. Due to the high temperature required for Cu/Al_2O_3 to activate propene and oxygen, pure Cu should have significantly higher activation energy than pure Pt and PtCu samples. The high energy barrier on Cu can be correlated with the higher activation energy observed on the Cu-rich sample $Pt_{44}Cu_{56}/Al_2O_3$ (Figure 3b). Cu/Al_2O_3 on its own is much less active in this reaction, likely due to the inability to bind propene on an oxidized CuO/Cu_2O surface. Summarily, we observe that Pt_xCu_{100-x} alloys performed better than either individual monometallic catalyst.

To quantitatively understand the effects of Cu alloying with Pt, steady-state kinetic measurements were performed in the differential regime, and turnover frequencies (TOFs) were calculated based on CO chemisorption values (Figure 3b and Figure S3). The $Pt_{86}Cu_{14}/Al_2O_3$ and $Pt_{69}Cu_{31}/Al_2O_3$ samples were found to have a TOF five and ten times greater than that of Pt/Al_2O_3, respectively. Even on a Pt-mass basis, the $Pt_{86}Cu_{14}/Al_2O_3$ and $Pt_{69}Cu_{31}/Al_2O_3$ catalysts showed catalytic rates that were four times higher than that of Pt/Al_2O_3 (Figure S3). $Pt_{69}Cu_{31}/Al_2O_3$ appeared to form the most active surface (highest TOF); however, $Pt_{69}Cu_{31}/Al_2O_3$ exposed less Pt on the surface (Table S2), making the overall conversion (Pt-mass-normalized activity, Figure S3) similar to $Pt_{86}Cu_{14}/Al_2O_3$. The $Pt_{44}Cu_{56}/Al_2O_3$ catalyst again showed lower activity. Given that the average NC diameter was held constant at ~5 nm in these materials and that the same Pt NC seeds were used in all cases, we infer that these differences were due to NC composition. These results indicate that it is possible to replace up to 30% of Pt with Cu and at the same time to achieve improved activity for propene combustion.. The reason that the $Pt_{69}Cu_{31}/Al_2O_3$ sample shows the highest TOF could be attributed to the fact that it exposes more active sites or forms a desired electronic structure with Cu to facilitate propene combustion; both aspects will be discussed below.

The Pt/Cu composition remains critical in determining whether catalytic activity is promoted or inhibited. While the

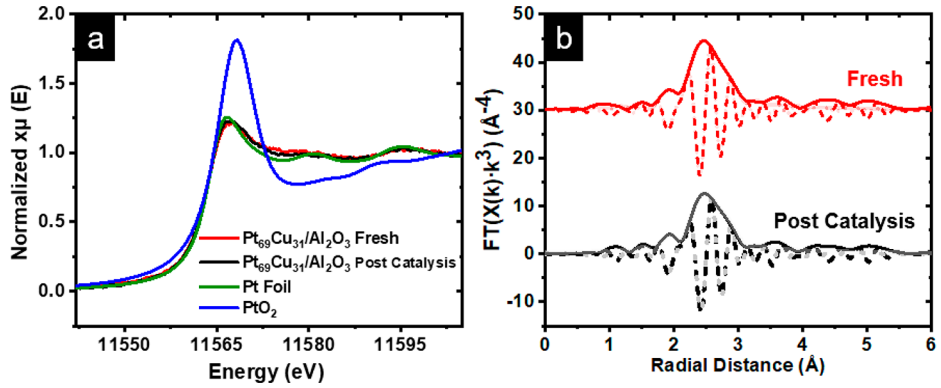

Figure 4. (a) Pt L_3-edge XANES for the $Pt_{69}Cu_{31}/Al_2O_3$ as prepared (fresh) and after catalysis along with Pt foil and PtO_2 references. (b) k^3-weighted Fourier transform EXAFS at the Pt L_3-edge with best fits for the $Pt_{69}Cu_{31}/Al_2O_3$ as prepared (fresh, upper red curve) and after catalysis (lower dark curve). The experimental data are presented with solid lines, and the imaginary components of the Fourier transform are presented with dashed lines and the corresponding fit models with light lines. Fit range: 1−3.4 Å.

Table 2. Best Fit EXAFS Results at the Pt L_3-Edge of the Air-Exposed $Pt_{69}Cu_{31}/Al_2O_3$ Sample before and after Catalysis[a]

	bond	CN	R [Å]	σ^2 [Å^2]	ΔE_0 [eV]	R factor (%)
fresh	Pt−Pt	7.2 ± 0.7	2.71 ± 0.03	0.0049 ± 0.0005	6.6 ± 0.5	1.3
	Pt−Cu	4.1 ± 0.8	2.67 ± 0.01	0.0091 ± 0.0016	6.6 ± 0.5	
post catalysis	Pt−Pt	6.9 ± 1.0	2.72 ± 0.02	0.0049 ± 0.0005	6.6 ± 0.5	1.3
	Pt−Cu	3.0 ± 0.9	2.69 ± 0.03	0.0091 ± 0.0016	6.6 ± 0.5	

[a]CN, coordination number; R, distance between absorber and backscattered atoms; σ^2, mean square disorder; ΔE_0, inner potential.

Pt/Al_2O_3, $Pt_{86}Cu_{14}/Al_2O_3$, and $Pt_{69}Cu_{31}/Al_2O_3$ catalysts have similar apparent activation energy values of 60, 65, and 53 kJ mol^{-1}, respectively, the $Pt_{44}Cu_{56}/Al_2O_3$ catalyst has a much higher value of 94 kJ mol^{-1}, which is consistent with the observed lower catalytic activity (Figure 3b; given the much lower activity, rates were not measured on Cu/Al_2O_3). Clearly, the addition of Cu to Pt improves its reactivity in a synergistic way, thus allowing us to use less Pt while boosting the catalyst activity further.

Reaction rate orders for propene and oxygen were measured to gain insight as to how Pt/Cu alloys promoted activity (Figure 3c,d). Propene rate order was found to be negative, while oxygen rate order was positive for all samples. These data indicate stronger propene adsorption on the metal surface and that propene and oxygen compete for available sites via a Langmuir−Hinshelwood mechanism,[49] in line with previous work on Pt/Al_2O_3.[17] Propene-adsorbed surfaces therefore determine the reactivity.[13] The propene rate order was more negative for $Pt_{69}Cu_{31}/Al_2O_3$ and $Pt_{86}Cu_{14}/Al_2O_3$ (−0.76 and −0.78) compared to Pt/Al_2O_3 and $Pt_{44}Cu_{56}/Al_2O_3$ (−0.44 and −0.48). Conversely, the oxygen rate order was more positive for $Pt_{86}Cu_{14}/Al_2O_3$ and $Pt_{86}Cu_{14}/Al_2O_3$ (1.02 and 1.10) than for Pt/Al_2O_3 and $Pt_{44}Cu_{56}/Al_2O_3$ (0.82 and 0.88). The trends on rate orders were in line with the rates and TOFs (Figure 3b): the more active samples showed higher sensitivity to the change in the partial pressures of propene and oxygen,[50] suggesting that the incorporation of Cu creates a surface with sites that bind propene more strongly, which requires oxygen to bind and activate on a propene-crowded surface. Such surfaces provide more facile propene activation and lower oxygen coverage, and we hypothesize that the more active PtCu surfaces are obtained by exposing more active sites (hypothetically the undercoordinated edge sites according to our previous work[13]) or that Cu may electronically modify Pt, with impacts on adsorbate binding.

The most active $Pt_{69}Cu_{31}/Al_2O_3$ bimetallic catalyst was characterized by X-ray absorption spectroscopy (XAS) at the Pt L_3-edge on both the fresh state and after propene combustion reaction. The X-ray absorption near-edge structure (XANES) spectra of the $Pt_{69}Cu_{31}/Al_2O_3$ samples (exposed to air) show that both the intensity and position of the white line are similar to those of the Pt foil standard (Figure 4a), indicating the presence of a predominantly metallic Pt state on both samples before and after reaction.

The best fit model of the extended X-ray absorption fine structure (EXAFS) data includes both a Pt−Cu and a Pt−Pt scattering path, with a starting Pt−Cu coordination number of 4.1 ± 0.8 that slightly decreases after catalysis to 3.0 ± 0.9; the Pt−Pt contribution remains constant before and after catalysis (Table 2). The determined bond lengths are in agreement with prior studies for similar Pt/Cu alloyed systems.[51,52] These results confirm the existence of a Pt/Cu alloy structure in both the fresh and spent $Pt_{69}Cu_{31}/Al_2O_3$ catalysts (Figure 4b and Figures S4 and S5). The STEM EDS map (Figure S6) and XPS (Figure S7) on the $Pt_{69}Cu_{31}/Al_2O_3$ sample show that Pt and Cu remain alloyed and that Pt maintains a metallic state after catalysis, supporting the EXAFS results. Furthermore, the random alloy structure on PtCu catalysts remains stable during catalysis since no significant phase segregation is observed based on nearly unchanged XPS spectra (Figure S7) and coordination numbers from EXAFS (Table 2). With the interest to determine the mixing behavior and alloying structure within this system, we applied a methodology developed by Frenkel et al. where EXAFS data were used to extract the Cowley short-range order parameter (defined by eq 1).[30−32] By extracting this mixing parameter on both the initial and final state of the $Pt_{69}Cu_{31}/Al_2O_3$ catalyst, it was noted that the intermetallic mixing behavior did not change with an $\alpha = 0$. This value indicates that the $Pt_{69}Cu_{31}/Al_2O_3$ system is a perfect random alloy,[53] indicating a random distribution of Pt and Cu species within the particle. This information indicates that for

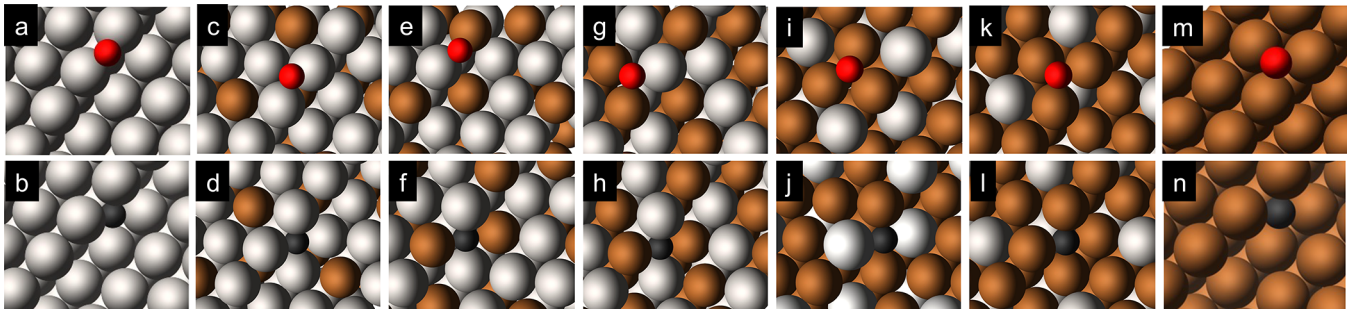

Figure 5. Surface structures of (a,b) Pt, (c,d) the Pt_3Cu–Pt step, (e,f) the Pt_3Cu-mixed step, (g,h) PtCu, (i,j) the $PtCu_3$-mixed step, (k,l) the $PtCu_3$–Cu step, and (m,n) Cu with oxygen and carbon adsorbates in their most stable adsorption geometry. Pt atoms are gray, Cu brown, O red, and C black.

either atom type, Pt or Cu, the probabilities for the neighboring atoms to consist of either Pt or Cu are equal.

Density functional theory (DFT) was used to investigate the impact of Cu on the adsorption strength of adsorbates on Pt and hence the reactivity of the catalyst. Pt_3Cu, PtCu, and $PtCu_3$ surfaces were modeled and compared to monometallic Pt and Cu surfaces. For the comparison, stepped face-centered cubic (211)-type surfaces were considered. These steps consist of 7-coordinated atoms and were found to be one of the major surface components for spherical FCC metals in the presence of steam and the most active sites that show lower activation barriers for propene combustion compared to the (111) counterpart.[13] Depending on the surface configuration, Pt_3Cu and $PtCu_3$ can have steps that consist of either only Pt, only Cu, or alternating Pt and Cu atoms. For PtCu, the step consists of alternating Pt and Cu atoms (Figure 5).

The adsorption energies of carbon and oxygen (C* and O*) were used as catalytic descriptors.[54] Among the different geometric configurations tested (top, bridge, hollow, and 4-fold sites), Table 3 reports the most stable adsorption energies for both adsorbates on several surfaces, and Figure 5 shows the most stable adsorption geometries. Adsorption energies are given relative to CH_4, H_2, and H_2O, and hence numbers are positive—lower values represent stronger adsorption.

Table 3. Calculated Adsorption Energies of the Catalytic Descriptors C* and O* on (211)-Type Surfaces of Pt, Cu, and Alloys thereof[a]

material	step composition	C* adsorption energy/eV	O* adsorption energy/eV
Pt	Pt step	2.18	1.20
Pt_3Cu	Pt step	2.20	1.31
	mixed step	2.49	1.28
PtCu	mixed step	2.14	1.30
$PtCu_3$	mixed step	2.70	1.22
	Cu step	3.25	1.24
Cu	Cu step	3.55	0.79

[a]Adsorption energies are given relative to CH_4, H_2, and H_2O.

Pt binds carbon more strongly than Cu does (C* of 2.2 eV vs 3.55 eV, respectively), while Cu binds oxygen more strongly than Pt (O* of 0.79 eV vs 1.20 eV, respectively). It is therefore expected that the addition of Cu into Pt would cause oxygen to bind more strongly and carbon to bind more weakly. As propene combustion is sensitive to the coverage and reactivity of O*,[55] adding too much Cu to Pt can result in unreactive O* and oxygen poisoning for a sample that has a Cu-like surface (i.e., Cu content significantly larger than 50%). For the PtCu as well as for both Pt_3Cu surface configurations, however, it was calculated that O* was slightly weakened, from 1.2 to 1.3 eV, while it remained almost unaltered compared to Pt for $PtCu_3$. In the case of C*, the PtCu and Pt_3Cu surfaces with a Pt-only step were hardly affected by introducing Cu into the structure. On the mixed-step Pt_3Cu surface as well as on both $PtCu_3$ terminations, C* was weakened by 0.3–1 eV. This implies that Pt_3Cu, PtCu, and $PtCu_3$ surfaces are Pt-like (with O* adsorption energies similar to the Pt surface) and that alloying Pt and Cu causes Cu to maintain a metallic state and remain stable even after the reaction under oxidizing conditions, according to XPS and XAS data on the postcatalysis samples (Figure 1e and Figure S7). It is likely that more Cu-rich compositions would instead show increased oxidation of the Cu phase.

To further investigate the electronic modifications caused by incorporating Cu into the Pt structure, the d density of states (dDOS) projected onto the Pt and Cu step atoms (Figure S8) was calculated for the Pt, Pt_3Cu, PtCu, and Cu surfaces. For the Cu atoms integrated into the steps, it was observed that the shape of the *d*DOS and the d-band center position was basically unaffected. For the Pt atoms, however, an upward shift of the d-band center of up to 0.3 eV was observed as Cu atoms were included into the step and the Cu content of the structure was increased. In addition, the evolution of a bimodal distribution of the Pt-projected dDOS was observed. In general, an upward shift of the d-band center is expected to cause stronger adsorption due to a decreased filling of the metal–adsorbate antibonding states.[56] By the explicit calculations of the adsorption energies, however, it was found that O* was slightly weakened, and C* remained similar or was weakened as Cu was added (Table 3). This observation underlines that simply considering the d-band center to predict adsorption trends is insufficient.[57] The structure and the bimodal nature of the dDOS projected on Pt as well as the interaction with the adsorbate orbitals compensate for the upward shift of the d-band center. This compensation leads to the, at first sight, unexpected but observed modifications of C* and O*, in line with previous studies of C, N, and O adsorption on PdX alloys (X representing late transition metals).[57] In these studies, for example, for carbon adsorbed on PdAg, it was found that while the d-band center shifted higher in energy compared to Pd, at the same time the C_{2p}–Pd_{4d} antibonding states decreased in energy toward the Fermi level and became more occupied; as a result, the Pd–C bond was effectively weakened. It is likely that a similar effect occurs in the Pt/Cu system when Cu is added to Pt.

In a detailed microkinetic modeling study of propene combustion over Pd, our group recently showed that the oxygen binding strength is a key factor in efficiently catalyzing propene combustion.[55] Too strong oxygen binding led to poisoning of the catalytic surface, whereas too weak oxygen binding deprived the surface of oxygen. Oxygen is needed on the surface to facilitate dehydrogenation and C−C scission reactions along the combustion pathway. It is clear therefore that adding small amounts of Cu into Pt (≤50%) slightly weakened the oxygen binding strength of the Pt which lessened oxygen poisoning, leading to a more favorable surface oxygen coverage and bond-splitting assistance of adsorbed O* to increase the propene combustion activity of Pt. While the oxygen surface coverage is important, being able to adsorb propene is naturally also a prerequisite for propene combustion. We observe that small additions of Cu (≤50%) hardly affect the adsorption strength of carbon species on PtCu alloys (Table 3). Adding larger amounts of Cu (>50%) into Pt, however, consistently weakens the binding of carbon species to the surface and again slightly increases the O* adsorption strength (Table 3). This combination decreases the propene availability on the surface and thereby decreases the propene combustion rate. Therefore, these O* and C* adsorption energy trends of Pt_xCu_y alloys help to explain our experimental observations that there exists an optimum concentration of Cu alloyed into Pt, causing optimal surface coverages of both oxygen and carbon species, thereby achieving the observed synergistic effect in propene combustion (Figure 3a,b). The synergy is a two-way effect: from Pt's perspective, adding Cu increases Pt's specific activity, whereas from Cu's perspective, Pt helps Cu stay in a Pt-like state (with O* adsorption energy similar to Pt). Together, the two elements combine to achieve desired binding energies for propene and oxygen to improve reactivity.

CONCLUSIONS

In this work, we developed a tunable seed-mediated colloidal synthesis method to produce a set of uniform Pt_xCu_{100-x} nanocrystals with controlled composition. Using in-depth structural characterization techniques, we demonstrated the successful alloying of Pt and Cu in individual nanocrystals while controlling Pt/Cu ratio. By depositing these precisely synthesized colloidal NCs on high surface area alumina, we created a set of catalysts that allow us to investigate the effect of Pt_xCu_{100-x} composition on propene combustion. Catalytic characterization experiments revealed that some Pt/Cu alloys ($Pt_{86}Cu_{14}$ and $Pt_{69}Cu_{31}$) exhibited up to ten times higher turnover frequencies compared to monometallic Pt, an obvious synergistic effect relative to its individual metal catalysts. Reaction order measurements evidenced a stronger propene binding on catalysts with intermediate Pt/Cu ratios, which may be attributed to the electronic influence of alloying. DFT studies corroborated this finding, showing how alloying Pt and Cu together helps Cu stay in the Pt-like state while improving carbon and oxygen binding energy toward optimal values. In summary, this study provides a foundation for synthesizing tunable, uniform bimetallic nanocrystals and probing the structure−property relationship of the alloy catalysts, which makes it possible to reduce noble metal usage in emission control catalysts.

AUTHOR INFORMATION

Corresponding Author

Matteo Cargnello − *Department of Chemical Engineering and SUNCAT Center for Interface Science and Catalysis, Stanford University, Stanford, California 94305, United States;* orcid.org/0000-0002-7344-9031; Email: mcargnello@stanford.edu

Authors

Nadia Tahsini − *Department of Chemical Engineering and SUNCAT Center for Interface Science and Catalysis, Stanford University, Stanford, California 94305, United States; Department of Chemical Engineering, Massachusetts Institute of Technology, Cambridge, Massachusetts 02139, United States*

An-Chih Yang − *Department of Chemical Engineering and SUNCAT Center for Interface Science and Catalysis, Stanford University, Stanford, California 94305, United States*

Verena Streibel − *Department of Chemical Engineering and SUNCAT Center for Interface Science and Catalysis, Stanford University, Stanford, California 94305, United States; SLAC National Accelerator Laboratory, SUNCAT Center for Interface Science and Catalysis, Menlo Park, California 94025, United States;* orcid.org/0000-0002-7758-8610

Baraa Werghi − *Department of Chemical Engineering and SUNCAT Center for Interface Science and Catalysis, Stanford University, Stanford, California 94305, United States; SLAC National Accelerator Laboratory, SUNCAT Center for Interface Science and Catalysis, Menlo Park, California 94025, United States*

Emmett D. Goodman − *Department of Chemical Engineering and SUNCAT Center for Interface Science and Catalysis, Stanford University, Stanford, California 94305, United States*

Aisulu Aitbekova − *Department of Chemical Engineering and SUNCAT Center for Interface Science and Catalysis, Stanford University, Stanford, California 94305, United States*

Simon R. Bare − *SLAC National Accelerator Laboratory, SUNCAT Center for Interface Science and Catalysis, Menlo Park, California 94025, United States*

Yuejin Li − *BASF Corporation, Environmental Catalysis R&D and Application, Iselin, New Jersey 08830, United States*

Frank Abild-Pedersen − *SLAC National Accelerator Laboratory, SUNCAT Center for Interface Science and*

Catalysis, Menlo Park, California 94025, United States;
orcid.org/0000-0002-1911-074X

Notes

The authors declare no competing financial interest.

■ ACKNOWLEDGMENTS

This work was supported by the BASF Corporation through the California Research Alliance program. Part of this work was performed at the Stanford Nano Shared Facilities, supported by the National Science Foundation under Award ECCS-1542152. The computational part of this work was supported by the U.S. Department of Energy, Office of Science, Office of Basic Energy Sciences, Chemical Sciences, Geosciences, and Biosciences Division, Catalysis Science Program through the SUNCAT Center for Interface Science and Catalysis. Use of the Stanford Synchrotron Radiation Lightsource, SLAC National Accelerator Laboratory, is supported by the U.S. Department of Energy, Office of Science, Office of Basic Energy Sciences under Contract No. DE-AC02-76SF00515. Dr. Verena Streibel acknowledges financial support from the Alexander von Humboldt Foundation. Dr. Adam S. Hoffman (SSRL and SLAC National Laboratory) is acknowledged for help in collecting the DRIFTS data. Dr. Ansgar Schäfer (BASF) and Dr. Roel Sanchez (BASF) are acknowledged for discussions on the data presented in this manuscript. Dr. Karen Bustillo (Lawrence Berkeley National Laboratory) is acknowledged for help and discussions on the STEM-EDS data. Work at the Molecular Foundry was supported by the Office of Science, Office of Basic Energy Sciences, of the U.S. Department of Energy under Contract No. DE-AC02-05CH11231.

■ REFERENCES

(1) Åhman, M.; Nilsson, L. J.; Johansson, B. Global Climate Policy and Deep Decarbonization of Energy-Intensive Industries. *Clim. Policy* **2017**, *17* (5), 634−649.

(2) Ojala, S.; Pitkäaho, S.; Laitinen, T.; Niskala Koivikko, N.; Brahmi, R.; Gaálová, J.; Matejova, L.; Kucherov, A.; Päivärinta, S.; Hirschmann, C.; Nevanperä, T.; Riihimäki, M.; Pirilä, M.; Keiski, R. L. Catalysis in VOC Abatement. *Top. Catal.* **2011**, *54* (16), 1224.

(3) Kao, A. S. Formation and Removal Reactions of Hazardous Air Pollutants. *Air Waste* **1994**, *44* (5), 683−696.

(4) Datye, A. K.; Votsmeier, M. Opportunities and Challenges in the Development of Advanced Materials for Emission Control Catalysts. *Nat. Mater.* **2021**, *20* (8), 1049−1059.

(5) He, C.; Cheng, J.; Zhang, X.; Douthwaite, M.; Pattisson, S.; Hao, Z. Recent Advances in the Catalytic Oxidation of Volatile Organic Compounds: A Review Based on Pollutant Sorts and Sources. *Chem. Rev.* **2019**, *119* (7), 4471−4568.

(6) Zhang, Z.; Jiang, Z.; Shangguan, W. Low-Temperature Catalysis for VOCs Removal in Technology and Application: A State-of-the-Art Review. *Catal. Today* **2016**, *264*, 270−278.

(7) Liotta, L. F. Catalytic Oxidation of Volatile Organic Compounds on Supported Noble Metals. *Appl. Catal. B Environ.* **2010**, *100*, 403−412.

(8) Carlsson, P.-A.; Skoglundh, M. Low-Temperature Oxidation of Carbon Monoxide and Methane over Alumina and Ceria Supported Platinum Catalysts. *Appl. Catal. B Environ.* **2011**, *101* (3), 669−675.

(9) Barakat, T.; Rooke, J. C.; Tidahy, H. L.; Hosseini, M.; Cousin, R.; Lamonier, J.-F.; Giraudon, J.-M.; De Weireld, G.; Su, B.-L.; Siffert, S. Noble-Metal-Based Catalysts Supported on Zeolites and Macro-Mesoporous Metal Oxide Supports for the Total Oxidation of Volatile Organic Compounds. *ChemSusChem* **2011**, *4* (10), 1420−1430.

(10) Verma, A.; Kore, R.; Corbin, D. R.; Shiflett, M. B. Metal Recovery Using Oxalate Chemistry: A Technical Review. *Ind. Eng. Chem. Res.* **2019**, *58* (34), 15381−15393.

(11) Zhang, Q.; Wu, L.; Fang, X.; Liu, M.; Zhang, J.; Shao, M.; Lu, S.; Mao, H. Emission Factors of Volatile Organic Compounds (VOCs) Based on the Detailed Vehicle Classification in a Tunnel Study. *Sci. Total Environ.* **2018**, *624*, 878−886.

(12) Aznarez, A.; Gil, A.; Korili, S. A. Performance of Palladium and Platinum Supported on Alumina Pillared Clays in the Catalytic Combustion of Propene. *RSC Adv.* **2015**, *5*, 82296−82309.

(13) Yang, A.-C.; Choksi, T.; Streibel, V.; Aljama, H.; Wrasman, C. J.; Roling, L. T.; Goodman, E. D.; Thomas, D.; Bare, S. R.; Sánchez-Carrera, R. S.; Schäfer, A.; Li, Y.; Abild-Pedersen, F.; Cargnello, M. Revealing the Structure of a Catalytic Combustion Active-Site Ensemble Combining Uniform Nanocrystal Catalysts and Theory Insights. *Proc. Natl. Acad. Sci. U. S. A.* **2020**, *117* (26), 14721−14729.

(14) Hansen, T. K.; Høj, M.; Hansen, B. B.; Janssens, T. V. W.; Jensen, A. D. The Effect of Pt Particle Size on the Oxidation of CO, C_3H_6, and NO Over Pt/Al_2O_3 for Diesel Exhaust Aftertreatment. *Top. Catal.* **2017**, *60*, 1333−1344.

(15) Carballo, L. M.; Wolf, E. E. Crystallite Size Effects during the Catalytic Oxidation of Propylene on Pt/γ-Al_2O_3. *J. Catal.* **1978**, *53*, 366−373.

(16) Baylet, A.; Capdeillayre, C.; Retailleau, L.; Valverde, J. L.; Vernoux, P.; Giroir-Fendler, A. Parametric Study of Propene Oxidation over Pt and Au Catalysts Supported on Sulphated and Unsulphated Titania. *Appl. Catal. B Environ.* **2011**, *102*, 180−189.

(17) Avila, M. S.; Vignatti, C. I.; Apesteguía, C. R.; Garetto, T. F. Effect of Support on the Deep Oxidation of Propane and Propylene on Pt-Based Catalysts. *Chem. Eng. J.* **2014**, *241*, 52−59.

(18) Hazlett, M. J.; Moses-Debusk, M.; Parks, J. E.; Allard, L. F.; Epling, W. S. Kinetic and Mechanistic Study of Bimetallic Pt-Pd/Al_2O_3 Catalysts for CO and C3H6 Oxidation. *Appl. Catal. B Environ.* **2017**, *202*, 404−417.

(19) Haneda, M.; Suzuki, K.; Sasaki, M.; Hamada, H.; Ozawa, M. Catalytic Performance of Bimetallic $PtPd/Al_2O_3$ for Diesel Hydrocarbon Oxidation and Its Implementation by Acidic Additives. *Appl. Catal. A Gen.* **2014**, *475*, 109−115.

(20) Goodman, E. D.; Dai, S.; Yang, A.-C.; Wrasman, C. J.; Gallo, A.; Bare, S. R.; Hoffman, A. S.; Jaramillo, T. F.; Graham, G. W.; Pan, X.; Cargnello, M. Uniform Pt/Pd Bimetallic Nanocrystals Demonstrate Platinum Effect on Palladium Methane Combustion Activity and Stability. *ACS Catal.* **2017**, *7*, 4372−4380.

(21) Willis, J. J.; Gallo, A.; Sokaras, D.; Aljama, H.; Nowak, S. H.; Goodman, E. D.; Wu, L.; Tassone, C. J.; Jaramillo, T. F.; Abild-Pedersen, F.; Cargnello, M. Systematic Structure−Property Relationship Studies in Palladium-Catalyzed Methane Complete Combustion. *ACS Catal.* **2017**, *7* (11), 7810−7821.

(22) Mu, R.; Fu, Q.; Xu, H.; Zhang, H.; Huang, Y.; Jiang, Z.; Zhang, S.; Tan, D.; Bao, X. Synergetic Effect of Surface and Subsurface Ni Species at Pt−Ni Bimetallic Catalysts for CO Oxidation. *J. Am. Chem. Soc.* **2011**, *133* (6), 1978−1986.

(23) Chen, G.; Zhao, Y.; Fu, G.; Duchesne, P. N.; Gu, L.; Zheng, Y.; Weng, X.; Chen, M.; Zhang, P.; Pao, C.-W.; Lee, J.-F.; Zheng, N. Interfacial Effects in Iron-Nickel Hydroxide−Platinum Nanoparticles Enhance Catalytic Oxidation. *Science (80-.).* **2014**, *344* (6183), 495−499.

(24) Komatsu, T.; Takasaki, M.; Ozawa, K.; Furukawa, S.; Muramatsu, A. PtCu Intermetallic Compound Supported on Alumina Active for Preferential Oxidation of CO in Hydrogen. *J. Phys. Chem. C* **2013**, *117* (20), 10483−10491.

(25) Li, Y.-N.; Xie, Y.-B.; Liu, C.-J. Enhanced Activity of Bimetallic Pd-Based Catalysts for Methane Combustion. *Catal. Lett.* **2008**, *125* (1), 130−133.

(26) Wu, L.; Fournier, A. P.; Willis, J. J.; Cargnello, M.; Tassone, C. J. In Situ X-Ray Scattering Guides the Synthesis of Uniform PtSn Nanocrystals. *Nano Lett.* **2018**, *18* (6), 4053−4057.

(27) Cargnello, M.; Chen, C.; Diroll, B. T.; Doan-Nguyen, V. V. T.; Gorte, R. J.; Murray, C. B. Efficient Removal of Organic Ligands from Supported Nanocrystals by Fast Thermal Annealing Enables Catalytic Studies on Well-Defined Active Phases. *J. Am. Chem. Soc.* **2015**, *137*, 6906−6911.
(28) Cliff, G.; Lorimer, G. W. The Quantitative Analysis of Thin Specimens. *J. Microsc.* **1975**, *103* (2), 203−207.
(29) Ravel, B.; Newville, M. ATHENA, ARTEMIS, HEPHAESTUS: Data Analysis for X-Ray Absorption Spectroscopy Using IFEFFIT. *J. Synchrotron Radiat.* **2005**, *12* (4), 537−541.
(30) Frenkel, A. I. Applications of Extended X-Ray Absorption Fine-Structure Spectroscopy to Studies of Bimetallic Nanoparticle Catalysts. *Chem. Soc. Rev.* **2012**, *41* (24), 8163−8178.
(31) Frenkel, A. I.; Wang, Q.; Sanchez, S. I.; Small, M. W.; Nuzzo, R. G. Short Range Order in Bimetallic Nanoalloys: An Extended X-Ray Absorption Fine Structure Study. *J. Chem. Phys.* **2013**, *138* (6), 64202.
(32) McGuire, S. C.; Ebrahim, A. M.; Hurley, N.; Zhang, L.; Frenkel, A. I.; Wong, S. S. Reconciling Structure Prediction of Alloyed, Ultrathin Nanowires with Spectroscopy. *Chem. Sci.* **2021**, *12* (20), 7158−7173.
(33) Giannozzi, P.; Baroni, S.; Bonini, N.; Calandra, M.; Car, R.; Cavazzoni, C.; Ceresoli, D.; Chiarotti, G. L.; Cococcioni, M.; Dabo, I.; et al. QUANTUM ESPRESSO: A Modular and Open-Source Software Project for Quantum Simulations of Materials. *J. Phys.: Condens. Matter* **2009**, *21*, 395502.
(34) Hjorth Larsen, A.; Jørgen Mortensen, J.; Blomqvist, J.; Castelli, I. E.; Christensen, R.; Dułak, M.; Friis, J.; Groves, M. N.; Hammer, B.; Hargus, C.; Hermes, E. D.; Jennings, P. C.; Bjerre Jensen, P.; Kermode, J.; Kitchin, J. R.; Leonhard Kolsbjerg, E.; Kubal, J.; Kaasbjerg, K.; Lysgaard, S.; Bergmann Maronsson, J.; Maxson, T.; Olsen, T.; Pastewka, L.; Peterson, A.; Rostgaard, C.; Schiøtz, J.; Schütt, O.; Strange, M.; Thygesen, K. S.; Vegge, T.; Vilhelmsen, L.; Walter, M.; Zeng, Z.; Jacobsen, K. W. The Atomic Simulation Environment—a Python Library for Working with Atoms. *J. Phys.: Condens. Matter* **2017**, *29* (27), 273002.
(35) Wellendorff, J.; Lundgaard, K. T.; Møgelhøj, A.; Petzold, V.; Landis, D. D.; Nørskov, J. K.; Bligaard, T.; Jacobsen, K. W. Density Functionals for Surface Science: Exchange-Correlation Model Development with Bayesian Error Estimation. *Phys. Rev. B* **2012**, *85*, 235149.
(36) Vanderbilt, D. Soft Self-Consistent Pseudopotentials in a Generalized Eigenvalue Formalism. *Phys. Rev. B* **1990**, *41* (11), 7892−7895.
(37) Monkhorst, H. J.; Pack, J. D. Special Points for Brillouin-Zone Integrations. *Phys. Rev. B* **1976**, *13* (12), 5188−5192.
(38) Jain, A.; Ong, S. P.; Hautier, G.; Chen, W.; Richards, W. D.; Dacek, S.; Cholia, S.; Gunter, D.; Skinner, D.; Ceder, G.; Persson, K. A. Commentary: The Materials Project: A Materials Genome Approach to Accelerating Materials Innovation. *APL Mater.* **2013**, *1* (1), 11002.
(39) Bengtsson, L. Dipole Correction for Surface Supercell Calculations. *Phys. Rev. B* **1999**, *59* (19), 12301−12304.
(40) Christensen, R.; Hansen, H. A.; Vegge, T. Identifying Systematic DFT Errors in Catalytic Reactions. *Catal. Sci. Technol.* **2015**, *5* (11), 4946−4949.
(41) Studt, F.; Behrens, M.; Kunkes, E. L.; Thomas, N.; Zander, S.; Tarasov, A.; Schumann, J.; Frei, E.; Varley, J. B.; Abild-Pedersen, F.; Nørskov, J. K.; Schlögl, R. The Mechanism of CO and CO_2 Hydrogenation to Methanol over Cu-Based Catalysts. *ChemCatChem.* **2015**, *7* (7), 1105−1111.
(42) Momma, K.; Izumi, F. VESTA3 for Three-Dimensional Visualization of Crystal, Volumetric and Morphology Data. *J. Appl. Crystallogr.* **2011**, *44* (6), 1272−1276.
(43) Saravanan, G.; Khobragade, R.; Chand Nagar, L.; Labhsetwar, N. Ordered Intermetallic Pt−Cu Nanoparticles for the Catalytic CO Oxidation Reaction. *RSC Adv.* **2016**, *6* (88), 85634−85642.
(44) Wahab, M. A. Necessity of Two More Space Lattices. *arXiv* **2009**, *0906*, 1358.
(45) Rumble, J. R., Jr.; Bickham, D. M.; Powell, C. J. The NIST X-Ray Photoelectron Spectroscopy Database. *Surf. Interface Anal.* **1992**, *19* (1−12), 241−246.
(46) Rodriguez, J. A.; Truong, C. M.; Goodman, D. W. Infrared Vibrational Studies of CO Adsorption on Cu/Pt(111) and CuPt(111) Surfaces. *J. Chem. Phys.* **1992**, *96* (10), 7814−7825.
(47) Abild-Pedersen, F.; Andersson, M. P. CO Adsorption Energies on Metals with Correction for High Coordination Adsorption Sites − A Density Functional Study. *Surf. Sci.* **2007**, *601* (7), 1747−1753.
(48) Sandell, A.; Bennich, P.; Nilsson, A.; Hernnäs, B.; Björneholm, O.; Mårtensson, N. Chemisorption of CO on Cu(100), Ag(110) and Au(110). *Surf. Sci.* **1994**, *310* (1), 16−26.
(49) Benard, S.; Baylet, A.; Vernoux, P.; Valverde, J. L.; Giroir-Fendler, A. Kinetics of the Propene Oxidation over a Pt/Alumina Catalyst. *Catal. Commun.* **2013**, *36*, 63−66.
(50) Morooka, Y.; Ozaki, A. Regularities in Catalytic Properties of Metal Oxides in Propylene Oxidation. *J. Catal.* **1966**, *5*, 116−124.
(51) Kaito, T.; Tanaka, H.; Mitsumoto, H.; Sugawara, S.; Shinohara, K.; Ariga, H.; Uehara, H.; Takakusagi, S.; Asakura, K. In Situ X-Ray Absorption Fine Structure Analysis of PtCo, PtCu, and PtNi Alloy Electrocatalysts: The Correlation of Enhanced Oxygen Reduction Reaction Activity and Structure. *J. Phys. Chem. C* **2016**, *120* (21), 11519−11527.
(52) Zhang, X.; Cui, G.; Feng, H.; Chen, L.; Wang, H.; Wang, B.; Zhang, X.; Zheng, L.; Hong, S.; Wei, M. Platinum−Copper Single Atom Alloy Catalysts with High Performance towards Glycerol Hydrogenolysis. *Nat. Commun.* **2019**, *10* (1), 5812.
(53) Timoshenko, J.; Wrasman, C. J.; Luneau, M.; Shirman, T.; Cargnello, M.; Bare, S. R.; Aizenberg, J.; Friend, C. M.; Frenkel, A. I. Probing Atomic Distributions in Mono- and Bimetallic Nanoparticles by Supervised Machine Learning. *Nano Lett.* **2019**, *19* (1), 520−529.
(54) Abild-Pedersen, F.; Greeley, J.; Studt, F.; Rossmeisl, J.; Munter, T. R.; Moses, P. G.; Skúlason, E.; Bligaard, T.; Nørskov, J. K. Scaling Properties of Adsorption Energies for Hydrogen-Containing Molecules on Transition-Metal Surfaces. *Phys. Rev. Lett.* **2007**, *99* (1), 16105.
(55) Streibel, V.; Aljama, H.; Yang, A.-C.; Sanchez, R.; Choksi, T.; Schäfer, A.; Li, Y.; Cargnello, M.; Abild-Pedersen, F. Microkinetic modeling of propene combustion on a stepped, metallic palladium surface and the importance of oxygen coverage. *ACS Catal.* **2021**, in press, DOI: 10.1021/acscatal.1c03699.
(56) Hammer, B.; Norskov, J. K. Why Gold Is the Noblest of All the Metals. *Nature* **1995**, *376* (6537), 238−240.
(57) Xin, H.; Vojvodic, A.; Voss, J.; Nørskov, J. K.; Abild-Pedersen, F. Effects of *d*-Band Shape on the Surface Reactivity of Transition-Metal Alloys. *Phys. Rev. B* **2014**, *89* (11), 115114.